Journal of Energy Chemistry 105 (2025) 142–157

Contents lists available at ScienceDirect

Journal of Energy Chemistry

journal homepage: www.elsevier.com/locate/jechem

http://www.journals.elsevier.com/journal-of-energy-chemistry/

Sensorless battery expansion estimation using electromechanical coupled models and machine learning

Xue Cai [a,b,c,d], Caiping Zhang [a,*], Jue Chen [b,c,d], Zeping Chen [a], Linjing Zhang [a], Dirk Uwe Sauer [b,c,d,e], Weihan Li [b,c,d,*]

[a] National Active Distribution Network Technology Research Center, Beijing Jiaotong University, Beijing 100044, China
[b] Institute for Power Electronics and Electrical Drives (ISEA), RWTH Aachen University, Campus Boulevard 89, 52074 Aachen, Germany
[c] Center for Ageing, Reliability and Lifetime Prediction of Electrochemical and Power Electronic Systems (CARL), Campus-Boulevard 89, 52074 Aachen, Germany
[d] Juelich Aachen Research Alliance, JARA-Energy, 52056 Aachen, Germany
[e] Helmholtz Institute Münster (HI MS), IMD-4, Forschungszentrum Jülich, 52425 Jülich, Germany

ARTICLE INFO

Article history:
Received 23 November 2024
Revised 13 December 2024
Accepted 15 December 2024
Available online 24 January 2025

Keywords:
Sensorless estimation
Electromechanical coupling
Impedance model
Data-driven model
Mechanical pressure

ABSTRACT

Developing sensorless techniques for estimating battery expansion is essential for effective mechanical state monitoring, improving the accuracy of digital twin simulation and abnormality detection. Therefore, this paper presents a data-driven approach to expansion estimation using electromechanical coupled models with machine learning. The proposed method integrates reduced-order impedance models with data-driven mechanical models, coupling the electrochemical and mechanical states through the state of charge (SOC) and mechanical pressure within a state estimation framework. The coupling relationship was established through experimental insights into pressure-related impedance parameters and the nonlinear mechanical behavior with SOC and pressure. The data-driven model was interpreted by introducing a novel swelling coefficient defined by component stiffnesses to capture the nonlinear mechanical behavior across various mechanical constraints. Sensitivity analysis of the impedance model shows that updating model parameters with pressure can reduce the mean absolute error of simulated voltage by 20 mV and SOC estimation error by 2%. The results demonstrate the model's estimation capabilities, achieving a root mean square error of less than 1 kPa when the maximum expansion force is from 30 kPa to 120 kPa, outperforming calibrated stiffness models and other machine learning techniques. The model's robustness and generalizability are further supported by its effective handling of SOC estimation and pressure measurement errors. This work highlights the importance of the proposed framework in enhancing state estimation and fault diagnosis for lithium-ion batteries.

1. Introduction

Lithium-ion batteries (LIBs) are widely used in various portable electronic devices, electric vehicles, and energy storage stations as an efficient energy storage device due to their outstanding performance [1–3]. However, LIBs were subjected to external pressure and internal expansion stress due to specific mechanical constraints, such as rigid [4], free [5], and flexible [6,7] bracing. These constraints affect both the short-term performance [5] and the long-term lifetime of LIBs [8]. For instance, high pressure not only undermines the energy/power capabilities of LIBs by reducing separator ionic conductivity and electrode active material surface area but also accelerates battery degradation by particle cracking [9]. In addition, mechanical expansion characteristics are promising for early failure detection, such as lithium plating [10], internal short-circuits [11], and thermal runaway [12,13], allowing more time for operational adjustments and safety measures.

To mitigate adverse pressure effects and leverage the benefits of mechanical-based fault detection, it is essential to obtain accurate expansion states, such as strain or stress. This information is crucial for optimizing the pressure range within battery packs and monitoring abnormal expansion growth. However, mechanical sensors like thin-film pressure sensors [14] and strain gauges [13] have yet to be widely adopted in mainstream battery systems due to their high costs, integration complexities, and concerns regarding operational reliability. These challenges will hinder the incorporation of mechanical sensors in battery modules or packs in the foreseeable future. The lack of mechanical expansion data

* Corresponding authors.
E-mail addresses: zhangcaiping@bjtu.edu.cn (C. Zhang), weihan.li@isea.rwth-aachen.de (W. Li).

https://doi.org/10.1016/j.jechem.2024.12.068

can delay failure warnings by over 500 s [12], significantly increasing the risk of personal injury and property damage from thermal runaways. Therefore, developing sensorless methods for estimating expansion is crucial for effectively monitoring the state of expansion (SOEx) in batteries and enhancing fault diagnosis through improved access to mechanical information.

The existing literature mainly focuses on battery expansion estimation methods based on mechanical models, including equivalent models [15–18] and data-driven models [19–22]. Equivalent models are categorized into linear elastic models (LEMs) and nonlinear elastic–plastic models (NLMs), depending on whether dynamic mechanical states under varying SOC, current rate, temperature, and other factors are taken into account. In LEMs, the spring stiffness of each component is calibrated through stress–strain compression experiments or estimated using swelling displacement and force measurements [23]. In contrast, NLMs involve more parameters and require higher sampling rates due to the introduction of damping elements and challenges in identifying relaxation effects.

However, the development of equivalent models faces three significant challenges: modeling theory, experimental methods, and parameter identifiability. The choice of model influences both the characterization experiments conducted and the identifiability of model parameters derived from these experiments. In LEM, compression tests on individual components often struggle with data matching between local and global objectives, leading to inaccurate parameter calibration. For NLMs, mechanical pulse characterization experiments at a given SOC – such as those designed by Jiang et al. [18] – can adversely affect the battery's mechanical performance at subsequent SOCs due to irreversible mechanical effects reported by Tobias et al. [24]. Furthermore, the identifiability of damping parameters relies heavily on high-precision thickness sensors with an accuracy of 0.1 μm and controlled pressure devices. These stringent equipment requirements present practical challenges for implementing NLMs. Additionally, as more influencing factors are considered, the necessary calibration experiments must also be scaled up significantly.

To address the challenges of large-scale parameter calibration, high-precision equipment, and multifactorial influences, data-driven mechanical models have shown considerable success in mechanical-based SOC estimation [19,20,25]. Xu et al. [19] developed a data-driven pressure model that accounts for the effects of current and SOC, where pressure serves as feedback information to adjust the Kalman gain for SOC estimation. This approach facilitates information fusion from two sensors to achieve closed-loop state estimation by utilizing data from other sensors as feedback. Similarly, Zhang et al. [26] demonstrated sensorless temperature estimation by leveraging voltage feedback simulated voltage from temperature-dependent electrical circuit models. These examples of closed-loop state estimations have inspired this research on battery expansion estimation through the feedback of additional signals. However, achieving initial pressure convergence using voltage feedback from an electromechanical coupled model within the extended Kalman filter (EKF) framework is challenging due to the significantly weaker electromechanical coupling compared to electrothermal coupled issues [27]. Consequently, battery expansion estimation remains primarily an open-loop problem. While converging initial pressure via EKF is deemed improbable, it is feasible to determine initial pressure through calibrated datasets by utilizing pressure-related model parameters such as ohmic resistance, interfacial resistance, and double-layer capacitance.

To date, battery expansion estimation still faces three challenges: multiple influencing factors, mechanical modeling theory, and estimation robustness. Regarding the factors influencing expansion states, existing studies still lack comprehensive insights into the factors influencing expansion characteristics due to limitations in mechanical characterization devices. Key aspects such as preload force – ranging from 30 to 200 kPa [4] – and realistic mechanical boundaries (e.g., free, rigid, and flexible brace conditions) are critical in determining battery expansion states, including expansion force and displacement. The generalization capability of data-driven models is frequently questioned in the context of multiple influencing factors and various machine learning algorithms [28,29]. Furthermore, a generalized mechanical modeling theory that addresses different mechanical boundaries to improve the model's physical explainability and guide adaptive mechanical simulations has yet to be developed. Additionally, discussions surrounding the estimation methods of data-driven mechanical models often overlook potential sources of error stemming from estimated SOC inaccuracies, model uncertainty, and measurement errors. Therefore, there is a pressing need for an adaptive data-driven mechanical model capable of operating under various mechanical boundaries to facilitate sensorless expansion estimation by accurately mapping nonlinear battery expansion characteristics.

To address the existing research gap, we propose a sensorless battery expansion estimation framework that integrates a data-driven approach with electromechanical coupled models, supported by a cloud-based battery management system (BMS). This framework involves constraint-based electrochemical-mechanical performance characterization and static compression tests to analyze the electromechanical behavior of the battery and determine the stiffness of each component within mechanical systems. We define a generalized swelling coefficient g by deriving mechanical constitutive equations under various mechanical boundary conditions, facilitating the transition from free or rigid to flexible bracing. Given the nonlinear swelling coefficient and non-monotonic electrochemical-induced mechanical behavior, we developed a data-driven mechanical model using least squares support vector regression (LSSVR) to simulate expansion swelling force under flexible bracing with varying stiffness. In terms of electrochemistry, frequency-domain impedance models were employed to quantify the effects of pressure on electrochemical kinetics, clarifying the electromechanically coupled relationship for terminal voltage through time-domain equivalent circuit modeling. Our framework incorporates multi-scale estimation processes, enabling short-term SOC estimation and long-term expansion estimation within an EFK framework. This includes a reduced-order impedance model and expansion curves sourced from cloud BMS for real-time field operations. The results demonstrate that our data-driven mechanical model significantly enhances the accuracy of simulated expansion force in both best-case and worst-case scenarios compared to traditional calibrated models. It also outperforms other machine learning methods, such as elastic net regression (ENR), random forest (RF), support vector regression (SVR), and Gaussian process regression (GPR). Specifically, parameters related to open-circuit voltage (OCV) and impedance enhance simulated voltage accuracy with a mean absolute error of 20 mV, and SOC estimation accuracy improved by 2%. The battery expansion estimation across different levels of estimation and measurement errors further demonstrates the robustness of the proposed data-driven mechanical model. These results underscore the potential effectiveness of our framework in achieving sensorless battery expansion estimation.

2. Experimental and battery expansion characteristics

Electrical and mechanical experiments were conducted on commercial LIB pouch cells under various bracing conditions. These cells operate within a voltage range of 2.50 to 4.20 V, with a maximum charge/discharge rate of 1.5 C and a nominal capacity of 50

Ah. The battery cell consists of a $LiNi_{0.8}Co_{0.1}Mn_{0.1}O_2$ (NCM811) cathode and a composite graphite-silicon oxide (Gr-SiO_x) anode. The dimensions of the cells are 291 mm × 100 mm (length × width), which were used for calculating compression stress. The experimental setup includes charge/discharge equipment (Arbin, LBT 5 V-100A), an in-situ swelling device (SWE2110, IEST), mechanical fixtures, and an electrochemical impedance spectroscopy device (Biologic, VMP-300). These devices are connected to a host computer for pressure control and data collection. The battery cell is linked through electrical and mechanical connections to control the applied current and compression force. The swelling behavior of the cell was monitored using high-precision pressure and displacement sensors integrated with an adaptive pressure regulation control system that operates in multiple modes: such as constant pressure mode (CPM), constant displacement mode (CDM), and variable displacement and pressure mode, i.e., flexible bracing mode (FBM), as illustrated in Fig. 1. A detailed description of the working principles of mechanical fixtures as well as the accuracy and resolution specifications of the sensors can be found in our previous study [27]. In CPM, changes in cell thickness are calculated by eliminating sensor deformation from the measured expansion data. The stress–strain relationship of load cells was calibrated using the following transient compression tests in Experiment IV.

Given the irreversible electrochemical effects and incomplete rebound mechanical effects of mechanical stress on LIBs, three cells were used for the following tests, assuming the consistency in swelling properties. Table 1 presents the details of the mechanical constraints and pressure values applied in each experiment, along with calibrated parameters from those experiments.

In Experiment I, we employed CPM to evaluate the pressure-induced swelling displacement ($\Delta\delta$) of the LIBs. The battery underwent charge and discharge cycles at rates of 0.1 C, 0.5 C, 1 C, and 1.5 C within a voltage range of 2.5 V to 4.2 V. Following a stabilization period of 5 h to minimize stress relaxation (initial stresses are listed in Table 1), the battery was charged using a constant current (CC) until it reaches 4.2 V, followed by a constant voltage (CV) phase until the current dropped to 0.1 C. The discharge process commenced at CC until reaching 2.5 V in the first phase, followed by a 1 h rest period before discharging at a rate of 0.05 C until fully depleting to 2.5 V again. This charge/discharge regimen is referred to as two-stage rate tests; for brevity, this procedure will not be repeated in subsequent experiments.

Experiment II involved pressurized cells operating under CDM. This experiment aimed to analyze how initial pressure impacts swelling force ($\Delta\sigma$) and subsequently estimate the stiffness of the battery cell. To eliminate variations due to current rates on swelling behavior, we used identical charge/discharge currents as in Experiment I: charging at 0.5C and discharging at 0.1C while implementing the FUDS driving cycle to compare static and dynamic expansion forces effectively.

Experiment III was conducted under CDM with the addition of a buffer layer made from pre-oxygenated silk fiber (YS) aerogel cushion to explore how this buffer layer affects the reduction of mechanical pressure transmitted from rigid endplates. This configuration is referred to as CDM + YS. In this experiment, the fully-discharged cell was pressurized to a target initial pressure value (σ_{init}) described in Table 2. Following this, the same current protocols used in Experiments I and II were applied to compare the swelling force induced by lithium intercalation under various mechanical boundaries. During the experiment, the cell was discharged at a rate of 0.1 C until it reached every 10% increment of its maximum capacity. After each discharge step, there was a 1-h rest period before repeating the process until reaching 2.5 V. This test procedure was adopted to characterize both electrical and mechanical performance caused by compression forces.

In Experiment IV, static compression tests were performed on the pressure sensor and buffer layer to calculate their respective stiffness values. The pressurization phase lasted for 30 s, followed by a regulating pressure process lasting 5 s.

To reveal the pressure dependency of cell mechanical behavior, we plotted the evolution of mechanical properties with SOC and initial pressures. Fig. 2 show swelling displacement and force under different pressures. It was observed that the change in pressure-related swelling force was significantly more pronounced than that in swelling displacement. This phenomenon can be attributed to the increased stiffness associated with higher pressures, alongside only minor changes in porosity. Fig. 2(c,d) depict the relationship between swelling displacement and force across different pressure levels. The curves are divided into three distinct regions during both expansion and contraction, based on volume changes driven by dominant phase transitions. Through incremental capacity analysis following cell balancing, as well as an examination of the swelling curve at the electrode level, our previous work has addressed these dominant phase transitions related to mechanical behavior [27]. In Region I, a slight slope is observed due to effects dominated by SiO_x, while a steeper slope is noted in Region II, resulting from graphite-dominated influences. Notably, the slope gradient increases with initial pressures, indicating an enhancement in stiffness as pressure rises. The contraction phenomenon observed in Region III is attributed to phase transitions within Nickel-rich cathodes transitioning from H_2 to H_3 [30,31]. Such highly nonlinear mechanical behavior poses significant challenges when calculating equivalent stiffness values, as previously reported by Kwak et al. [23]. These results provide compelling evidence for the effectiveness of the proposed data-driven model in addressing nonlinearity and non-monotonicity associated with both swelling coefficients and equivalent stiffness.

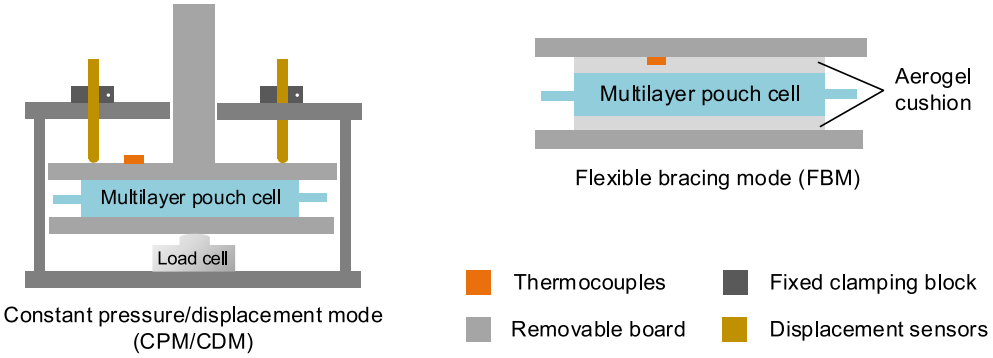

Fig. 1. Schematic diagram of the experimental platform.

Table 1
Calibration of relevant parameters from experiments under various mechanical constraints.

Mechanical constraint	Expansion coefficient	Cell No.	Pressure range (MPa)	Swelling thickness (mm)	Swelling force (kPa)	Stiffness (MPa)
CPM	$g = 1$	1	0.01 ~ 1.2	$\Delta\delta$	–	k_c
CDM	$g \sim= 0$	2	0.01 ~ 0.6	–	$\Delta\sigma$	
CDM + YS	$0 < g < 1$	3	0.01 ~ 0.4	–	$\Delta\sigma$	$k_c + k_s + k_b$

Table 2
Training and testing datasets used for the data-driven mechanical model.

Dataset	Initial pressure (MPa)	C-rate (C)	SOC (%)
#1	0.01, 0.02, 0.035, 0.05, 0.1, 0.15, 0.2, 0.25, 0.3, 0.35, 0.4	chg@0.5, chg@1, dis@0.1	0 ~ 100%
#2	0.015, 0.025, 0.03, 0.04,0.12,0.18,0.22,0.28,0.32,0.38	chg@0.5, chg@1, dis@0.1	0 ~ 100%

3. Methodology

The LIBs within modules or packs experience electromechanical coupling due to applied preload forces and mechanical boundaries, such as rigid or flexible bracing conditions. The intrinsic nonlinear characteristics of the materials add complexity to these electromechanical coupling problems. In Fig. 3, we propose a two-way electromechanical coupling model (EMCM) that recouples independent one-way modeling approaches to address the challenges of sensorless battery expansion estimation with the support of cloud BMS. The schematic diagram of the EMCM is shown in Fig. 4. Utilizing mechanical constitutive equations applicable under various bracing modes, we developed both force- and displacement-type mechanical models using calibrated data obtained from rigid or free expansion modes, along with swelling coefficients to simulate swelling force or displacement during charging and discharging processes. We opted for force-type mechanical models due to their compatibility with measurable force signals in experimental setups; however, the conceptual framework for displacement-type mechanical models remains applicable. The traditional swelling coefficient model was derived from the stiffness of each component and served as a benchmark method using calibrated stiffness values obtained from static stress–strain tests. In contrast, we employed a data-driven swelling coefficient model aimed at enhancing the understanding of the nonlinear and non-monotonic transformation relationship of swelling forces between rigid and flexible bracing modes. In Fig. 4, we established the EMCM by recoupling LSSVR-based mechanical models with pressure-dependent impedance models, where pressure and SOC connect two distinct physical domains. The LSSVR-based mechanical model utilizes load current and SOC information from the electrochemical impedance model alongside theoretical expansion forces derived from calibration datasets as inputs. The output of this model is the expansion force under FBM, which subsequently serves as input for updating parameters within the electrochemical impedance model in real-time – such as U_{oc} and impedance parameters – thereby simulating time-domain voltage responses under FUDS driving cycles. Given the complexities associated with real-world applications, we further explore model adaptation in field operations by considering factors such as sample errors, driving conditions, and loading states. The simulated results underscore the potential of our proposed model for co-simulating battery voltage and mechanical behavior across varying preload conditions and buffer assemblies, ultimately facilitating more accurate estimations of battery expansion states.

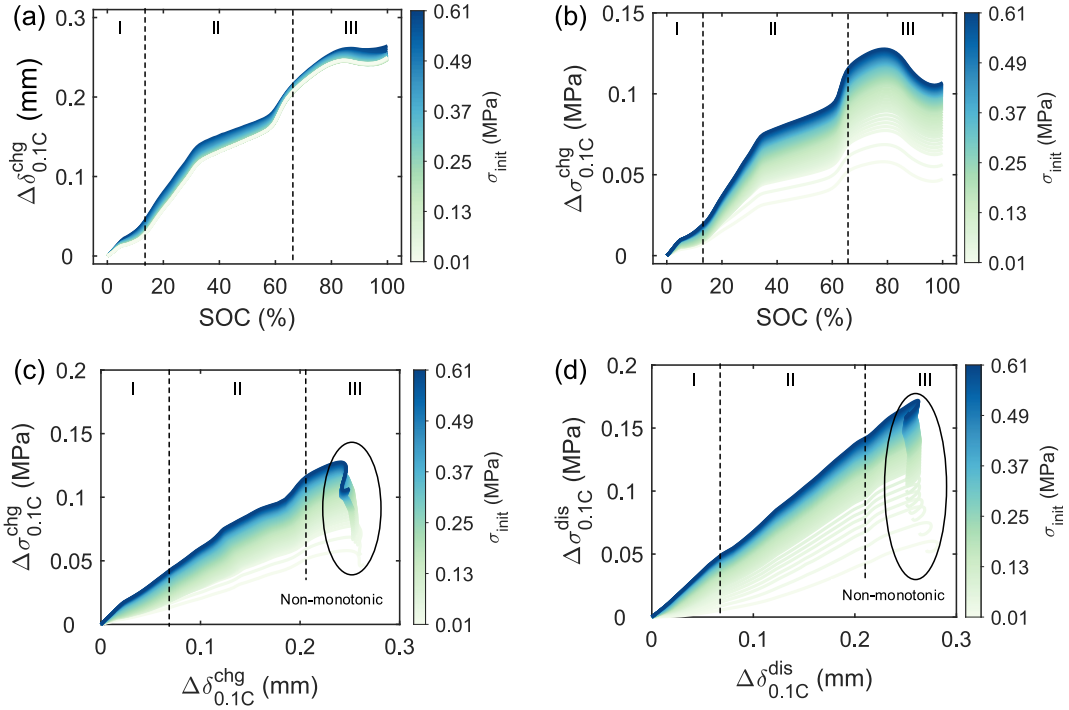

Fig. 2. Battery mechanical behavior analysis under mechanical constraints. (a) swelling displacement and (b) swelling force of 0.1 C charge with SOC and initial pressure. The relationship of (a) swelling stress and (b) thickness at 0.1C (c) charging and (d) discharging process.

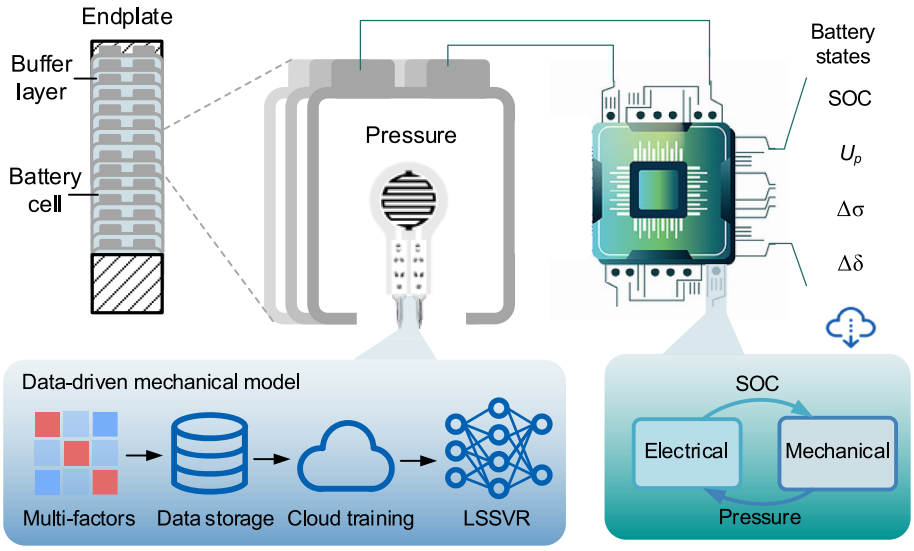

Fig. 3. Framework of battery expansion estimation through cloud-assisted EMCM.

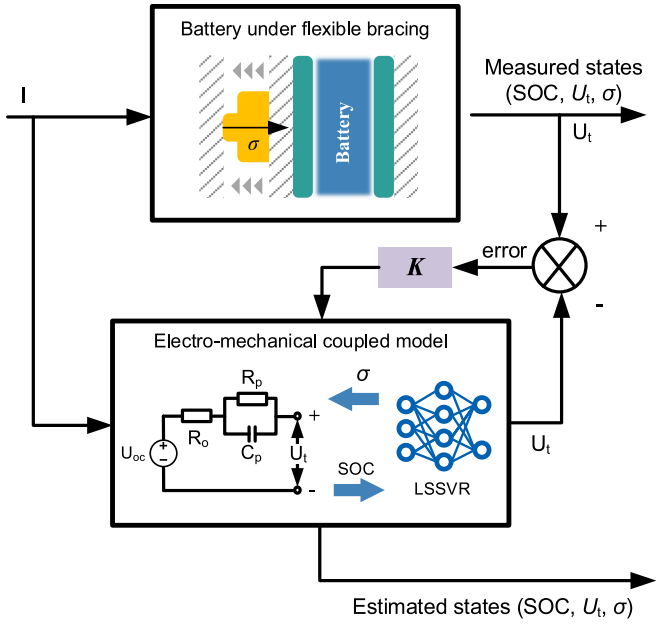

Fig. 4. Online state estimation based on electromechanical coupled model (EMCM).

3.1. Mechanical constitutive relationship under various bracing conditions

The cells typically undergo an initial preload and expansion force, considering the effects of the stacked battery pack and varying mechanical boundaries. As a flexible boundary, the buffer layer plays a crucial role by absorbing expansion thickness, thereby reducing the lithiation-induced reaction force. Thus, it is essential to develop an equivalent model that accurately captures variations in mechanical behavior under different stack pressures and flexible mechanical constraints. To this end, we measured the variation in battery mechanical behavior under preload conditions across different mechanical constraints, as illustrated in Fig. 1. It is important to note that the characteristics of viscous fluids were neglected due to their complex mechanisms and minimal responses during short-term relaxation periods. Thus, only the mechanical properties of elastic solids are considered in the subsequent derivations. Based on linear elastic theory, spring elements can effectively represent the mechanical properties of each component depicted in Fig. 5. The stress on these spring elements can be expressed as

$$\sigma = \frac{P}{A} \tag{1}$$

where P is the external force applied to the battery due to stack pressure within the battery pack, and A is the pressurized surface area. According to Hook's Law for force equilibrium, the constitutive relationship between stress and compressed thickness of the spring element is given by:

$$\begin{cases} \sigma_c = \sigma_b = \sigma_s = \sigma_0 + \Delta\sigma \\ \Delta\delta_i = k_i^{-1}\sigma_i, i = s, b, c \end{cases} \tag{2}$$

Here, σ_0 denotes initial stress, $\Delta\sigma$ represents expansion stress during the charge and discharge process, k and $\Delta\delta$ represent the stiffness and thickness variation of each element. The subscripts s, b, and c correspond to the pressure sensor, buffer layer, and cell. As shown in Fig. 1(c), both k_s and k_b can be calibrated using transient compression tests conducted in Experiment IV.

Considering the structure of porous electrode material, we can categorize the cell's mechanical properties into active material stiffness and pore volume stiffness. Thus, corresponding stiffness values and thickness changes for spring elements representing the cell are defined as follows:

$$k_c^{-1} = k_a^{-1} + k_p^{-1} \approx k_p^{-1} \tag{3}$$

$$\Delta\delta_c = \delta_{li,a} - \delta_p \tag{4}$$

where k_a and k_p represent the stiffness of active materials and pore volume, respectively. In Eq. (3), under certain assumptions – such as constant pore volume during unstrained swelling and negligible compression of active materials – the stiffness of battery cells (k_c) can be simplified primarily to pore volume stiffness (k_p). This simplification arises from recognizing that the stiffness of porous structures (< 10 MPa) is significantly lower than that of active materials (approx. 10 GPa) [32].

3.1.1. Mechanical constitutive equations under CPM

In elasticity theory, the force analysis of a series spring system involves establishing stress and strain equilibrium equations.

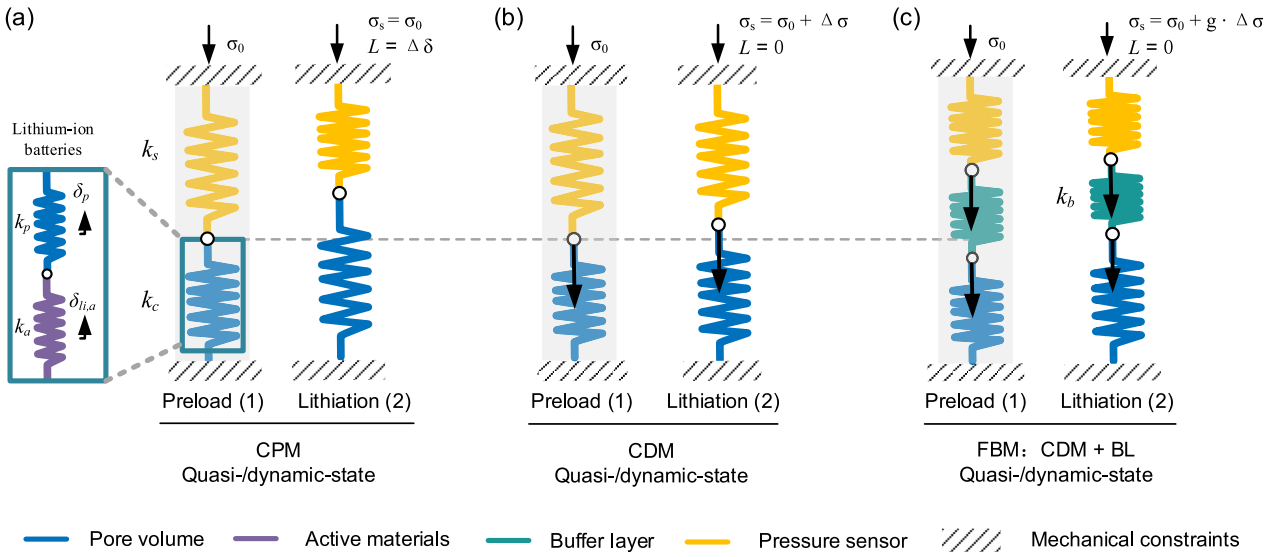

Fig. 5. Analysis of mechanical force and swelling for three cases. (a) intercalation-induced free swelling of the battery cell under constant mechanical constraints; (b) intercalation-induced free swelling under constant mechanical constraints; (c) intercalation-induced free swelling of the battery cell under constant mechanical constraints.

Specifically, stress equilibrium and geometric compatibility describe the constitutive relationship between stress and strain of each element within this series system. In Fig. 5(a), the stress equilibrium and geometric compatibility equation under CPM can be expressed as:

$$\begin{cases} \sigma_c = \sigma_s = \Delta\delta_s \cdot k_s \\ \Delta\delta_c = \delta_{li,a} = \delta_m + \Delta\delta_s \end{cases} \tag{5}$$

where σ is the current stress, equaling the measured σ_s; $\delta_{li,a}$ is the thickness variation induced by the lithiation process within the active materials; δ_p denotes the thickness change of the pore volume; and δ_m indicates the adjusted thickness of the servo-feedback motor required to maintain a constant pressure σ. During this control process, variations in thickness from the pressure sensor are compensated using a calibrated stress–strain curve from IEST 2110. Thus, the measured thickness reflects lithiation-induced changes at constant pressure as a function of stress and SOC, represented as $\delta_{li,a} = f(\sigma_{init}, \text{SOC}, \text{C})$, as shown in Fig. 2(a).

According to the constitutive equations outlined under CPM in Eq. (4) and (5), we summarize the compressed thickness ($\Delta\delta_c$) for two scenarios: (1) preloading conditions and (2) lithiation conditions.

$$\begin{cases} \Delta\delta_{c,0} = k_c^{-1}\sigma_s \\ \Delta\delta_c = \delta_{li,a} - \delta_p \end{cases} \tag{6}$$

Here, $\Delta\delta_{c,0}$ refers to compressed thickness during initial preload states when pore volume is also subjected to compression, as shown in the zoomed-in figure of Fig. 3(a). It should be noted that consistent values of δ_p at identical σ_s across various buffer conditions will not be further elaborated upon in the following sections. Importantly, no compression occurs in pore volume during lithiation due to maintained constant pressure; thus, $\delta_p = 0$ throughout charge or discharge processes. The measured CPM data, adjusted for sensor deformation effects, ultimately reflects theoretical expansion thickness ($\delta_{li,a}$) under different pressures.

3.1.2. Mechanical constitutive equations under CDM

Given the series spring system that encompasses the battery cell and pressure sensor, as depicted in Fig. 5(b), each spring element experiences the same compression force. Hence, the stress equilibrium and geometric compatibility equation for each element under CDM can be expressed as:

$$\begin{cases} \Delta\delta_c \cdot k_c = \Delta\delta_s \cdot k_s = \sigma_s \\ \delta_{li,a} - \delta_p + \Delta\delta_s = \Delta\delta_c + \Delta\delta_s = 0 \end{cases} \tag{7}$$

From Eq. (7), we can derive the stiffness of the cell as follows:

$$k_c^{-1} = \frac{\Delta\delta_c}{\sigma_s} = \frac{\delta_{li,a}(\sigma_s) - k_s^{-1}\sigma_s}{\sigma_s} \tag{8}$$

Here, mechanical stress σ_s modifies the theoretical expansion thickness under CDM. Thus, we can express $\Delta\delta_c$ during lithiation conditions based on Eq. (8). The stiffness and stress of the cell are calculated using $\Delta\delta_p$.

$$\Delta\delta_c = \delta_{li,a} - \delta_p = \delta_s = k_s^{-1}\sigma_s \tag{9}$$

In this context, when comparing Eq. (6) with Eq. (9), it is evident that more pore volume is compressed under CDM than under CPM. The compressed thickness of pore volume (δ_p) closely approximates the embedded lithium thickness of active materials ($\delta_{li,a}$). This observation arises because a pressure sensor with high stiffness experiences compression of less than 0.3 mm. To elucidate how rigid and flexible bracing conditions influence the mitigation of cell expansion under mechanical constraints, we define the equivalent stiffness of the CDM system (k_{CDM}) as follows:

$$k_{\text{CDM}}^{-1} = k_c^{-1} + k_s^{-1} \tag{10}$$

3.1.3. Mechanical constitutive equations under FBM

In Fig. 5(c), the series spring system consists of the battery cell, buffer layer, and pressure sensor, all subjected to the same compression force. The constitutive relationship between stress and strain for each element in this system can be expressed as:

$$\begin{cases} \Delta\delta_c \cdot k_c = \Delta\delta_b \cdot k_b = \Delta\delta_s \cdot k_s = \sigma_s \\ \delta_{li,a} - \delta_p + \Delta\delta_b + \Delta\delta_s = 0 \end{cases} \tag{11}$$

Using Eq. (11), we can derive the battery swelling displacement ($\Delta\delta_c$) during the lithiation process as follows:

$$\Delta\delta_c = \delta_{li,a} - \delta_p < \delta_{li,a} \tag{12}$$

when compared to Eq. (10), the stiffness of the FBM with buffer layer (BL) system can be represented as

$$k_{BL}^{-1} = k_c^{-1} + k_s^{-1} + k_b^{-1} > k_c^{-1} + k_s^{-1} \tag{13}$$

This expression illustrates that the stiffness of the equivalent system is reduced when spring elements are connected in series, particularly when comparing k_{eq} under CDM with and without a buffer layer. Furthermore, when examining Eqs. (5) and (7) alongside Eq. (11), it becomes apparent that $\Delta\delta_p$ lies between 0 and $\delta_{li,a}$ due to the cushioning capacity of the buffer layer in absorbing cell expansion.

3.2. Data-driven mechanical model by introducing swelling coefficient

3.2.1. Generalized swelling coefficient definition

To illustrate the evolution of mechanical behavior under various bracing conditions, we define a universal swelling coefficient (g) in Eq. (14), inspired by the work of Weidner and colleagues [33]. The swelling coefficient g quantifies the extent to which the battery cell can expand under specific mechanical conditions. For example, when g = 1, it indicates that the uncompressed pore volume is present in FSM and CPM. Conversely, when g approaches 0, it implies that the pore volume described in Eq. (15) is almost entirely compressed. The incompressibility of active materials determines that the pore volume remains consistently compressed during charging and discharging processes, except in FSM or CPM scenarios:

$$g_{CPM} = \frac{\Delta\delta_{c,CPM}}{\delta_{li,a}} = 1 \tag{14}$$

$$g_{CDM} = \frac{\Delta\delta_{c,CDM}}{\delta_{li,a}} = 1 - \frac{k_s^{-1}\sigma_{s,CDM}}{\delta_{li,a}} \approx 0 \tag{15}$$

$$g_{BL} = \frac{\Delta\delta_{c,BL}}{\delta_{li,a}} = \frac{k_{c,eq}^{-1}\sigma_{s,BL}}{\delta_{li,a}}, 0 < g_{BL} < 1 \tag{16}$$

where the subscripts for CPM, CDM, and BL denote pressurized modes without and with a buffer layer, respectively. To estimate $\Delta\sigma_{BL}$ by calibrated stiffness of each component, we substitute Eq. (16) into Eq. (11), then the equation set of g_{BL} and $\Delta\sigma_{BL}$ was given as:

$$\begin{cases} \delta_{li,a} \cdot g_{BL} = \left(k_s^{-1} + k_b^{-1}\right)\sigma_{s,BL} \\ k_c \cdot \delta_{li,a} \cdot (1 - g_{BL}) = \sigma_{s,BL} \end{cases} \tag{17}$$

By eliminating $\sigma_{s,\,BL}$, we can combine these equations into Eq. (17), allowing us to derive expressions for both $\sigma_{s,\,BL}$, and $\delta_{s,\,BL}$ under buffer layers with varying stiffnesses:

$$\begin{cases} \Delta\sigma_{s,BL} = (1 - g_{BL}) \cdot \Delta\sigma_{s,CDM} = \frac{k_c^{-1}(\sigma_s,z)}{k_c^{-1}(\sigma_s,z)+k_b^{-1}(\sigma_s)+k_s^{-1}(\sigma_s)} \cdot \Delta\sigma_{s,CDM} \\ \Delta\delta_{s,BL} = g_{BL} \cdot \Delta\delta_{s,CPM} = \frac{k_b^{-1}(\sigma_s)+k_s^{-1}(\sigma_s)}{k_c^{-1}(\sigma_s,z)+k_b^{-1}(\sigma_s)+k_s^{-1}(\sigma_s)} \cdot \Delta\delta_{s,CPM} \end{cases} \tag{18}$$

where the subscripts of CDM and BL denote pressurized mode without and with a buffer layer, respectively. Next, to enhance the accuracy of estimating $\Delta\sigma_{BL}$, we establish a data-driven model equivalent to the coefficient of g. We propose either a force- or displacement-type mechanical model as expressed in Eq. (18). This model incorporates calibrated data from CDM or CPM to simulate expansion force or displacement within preload and buffer assemblies. Thus, both force-type and displacement-type mechanical models are derived based on calibrated swelling forces under CDM and swelling displacements under CPM, as shown in Fig. S1 (a). In this work, we adopted a force-type mechanical model due to its compatibility with measurable forces in CDM and FBM mechanical fixtures. Therefore, establishing an adaptive mechanical model through data-driven methods becomes essential to account for nonlinear and non-monotonic stress relationships.

3.2.2. Force-type data-driven mechanical model via LSSVR

The LSSVR method proposed by Vandewalle [34] is applied in this work to a data-driven swelling model to address the non-monotonicity of the battery swelling coefficient and equivalent stiffness. LSSVR simplifies constraints by converting the convex quadratic optimization problem inherent in SVR into equality constraints, thus offering a more efficient solution for optimization challenges. It introduces the square error cost function to enhance the model's smoothness and robustness against noise. The LSSVR can be expressed as follows:

$$y_i = \sum_{i=1}^{N} a_i K(x_i, x_j) + b \tag{19}$$

The Radial basis function (RBF) is chosen as the kernel function due to its effectiveness in mitigating interference from noise and outliers. The RBF is defined as:

$$K(x_i, x_j) = \exp\left(-\frac{\| x_i - x_j \|}{\psi^2}\right) \tag{20}$$

where ψ is the kernel parameter. A more detailed calculation procedure can be found in [18].

Initially, we enhanced this dataset by interpolating calibrated results under the same initial pressure (σ_{init}) to eliminate discrepancies arising from variations in initial pressure across different C-rates and bracing modes. These calibrated results ($\Delta\sigma_{s,CDM}$ and $\Delta\sigma_{s,BL}$) were derived from CDM and FBM experiments based on SOC and σ_{init}. The enhanced datasets, i.e., #1 and #2, are summarized in Table 3. To further streamline our analysis while maintaining accuracy, we reduced the dataset size to 40 points by adjusting the SOC interval (e.g., 2.5%). Subsequently, we trained and validated the LSSVR model to simulate swelling force under specific initial pressures. As shown in Fig. S1(b), the input current, SOC, and theoretical expansion force $\Delta\sigma_{s,CDM}$ under σ_{init} is the most direct factor affecting $\Delta\sigma_{s,bl}$ by swelling coefficient. Therefore, these three variables were selected as the input vector, with expansion force under a specific buffer layer stiffness $k_b(\sigma)$ arranged as the output vector for the LSSVR model. The training dataset comprised 70% of dataset #1, while testing utilized 30% of dataset #1 and 100% of dataset #2. Leave-one-out cross-validation was implemented for performance evaluation to mitigate randomness associated with training on small sample datasets. In the training process of LSSVR, a simplex algorithm was used to adjust and optimize hyperparameters automatically. The resulting optimized values were 1078.53 for the regularization parameter and 0.1398 for the kernel parameter. Evaluation metrics for mechanical signals were based on several criteria: root mean square error (RMSE), maximum absolute error (MAE), and mean absolute percentage error (MAPE), defined as follows:

$$\mathrm{RMSE} = \sqrt{\frac{1}{N}\sum_{t=1}^{M}(\sigma_t - \hat{\sigma}_t)^2} \tag{21}$$

$$\mathrm{MAE} = \frac{1}{N}\sum_{t=1}^{N}|\sigma_t - \hat{\sigma}_t| \tag{22}$$

$$\mathrm{MAPE} = \frac{1}{N}\sum_{t=1}^{N}|(\sigma_t - \hat{\sigma}_t)/\sigma_t| * 100 \tag{23}$$

Table 3
Coefficient matrix of different fractional-order impedance models.

Models	m	n	Coefficient matrix
(RL)R(RQ)(RC)W	12	6	$\begin{cases} \alpha = \{\alpha_2, \alpha_2+1, \alpha_2+2, \alpha_1+\alpha_2, \alpha_1+\alpha_2+1, \alpha_1+\alpha_2+2\} \\ \beta = \begin{Bmatrix} \alpha_2, \alpha_2+1, \alpha_2+2, \alpha_1+\alpha_2, \alpha_1+\alpha_2+1, \dots \\ \alpha_1+\alpha_2+2, 0, 1, 2, \alpha_1, \alpha_1+1, \alpha_1+2 \end{Bmatrix} \\ a = \{1, \tau_e+\tau_L, \tau_e\tau_L, \tau_i^{\alpha_1}, (\tau_e+\tau_L)\tau_i^{\alpha_1}, \tau_e\tau_L\tau_i^{\alpha_1}\} \\ b = \begin{Bmatrix} R_i+R_e, L+R_i\tau_L+R_i\tau_e+R_e\tau_L, L\tau_e+R_i\tau_e\tau_L, \\ R_e\tau_i^{\alpha_1}, L\tau_i^{\alpha_1}+R_e\tau_L\tau_i^{\alpha_1}, L\tau_e\tau_i^{\alpha_1}, R_s, R_s(\tau_e+\tau_L), \\ R_s\tau_e\tau_L, R_s\tau_i^{\alpha_1}, R_s\tau_i^{\alpha_1}(\tau_e+\tau_L), R_s\tau_i^{\alpha_1}\tau_e\tau_L \end{Bmatrix} \end{cases}$
R(RQ)(RC)W	7	4	$\begin{cases} \alpha = \{\alpha_2, \alpha_1+\alpha_2, \alpha_2+1, \alpha_1+\alpha_2+1\} \\ \beta = \{\alpha_2, \alpha_2+1, 0, 1, \alpha_1, \alpha_1+1, \alpha_1+\alpha_2\} \\ a = \{1, \tau_i^{\alpha_1}, \tau_e, \tau_e\tau_i^{\alpha_1}\} \\ b = \{R_i+R_e, R_i\tau_e, R_s, R_s\tau_e, R_s\tau_i^{\alpha_1}, R_s\tau_e\tau_i^{\alpha_1}, R_e\tau_i^{\alpha_1}\} \end{cases}$
R(RQ)(RC)	3	4	$\begin{cases} \alpha = \{0, 1, \alpha_1, \alpha_1+1\} \\ \beta = \{0, 1, \alpha_1\} \\ a = \{1, \tau_e, \tau_i^{\alpha_1}, \tau_e\tau_i^{\alpha_1}\} \\ b = \{R_i+R_e, R_i\tau_e, R_e\tau_i^{\alpha_1}\} \end{cases}$
R(RQ)	1	2	$\begin{cases} \alpha = \{0, \alpha_1\} \\ \beta = \{0\} \\ a = \{1, \tau_i^{\alpha_1}\} \\ b = \{R_i\} \end{cases}$
R(RC)	1	2	$\begin{cases} \alpha = \{0, 1\} \\ \beta = \{0\} \\ a = \{1, \tau_e\} \\ b = \{R_e\} \end{cases}$

3.3. Impedance-based electromechanical coupled model

3.3.1. Electromechanical coupled modeling

Building on the findings related to pressure-induced electrochemical reactions from [23], this work employs a reduced-order electrochemical impedance model as the basic framework to explore how pressure-related model parameters influence battery terminal voltage and expansion force. We establish a two-way electromechanical coupled model by incorporating external stress. The battery SOC can be obtained by the ampere-hour integral method, expressed mathematically as:

$$SOC_t = SOC_0 + \frac{\eta \int_{t_0}^{t} I(t)dt}{3600 C_n(\sigma)} \tag{24}$$

The outputs of the model, specifically terminal voltage and pressure, can be calculated using polarization voltage derived from a time-domain pressure-dependent impedance model characterized by N fractional order networks. The relationship is given by:

$$\begin{cases} U_t = OCV + \sum_{i=1}^{N} U_{p,i} + I \cdot R_0 \\ \frac{d^{\alpha} U_{p,i}}{dt} = \frac{I}{C_{p,i}} - \frac{U_{p,i}}{R_{p,i} C_{p,i}} \end{cases} \tag{25}$$

where U_t and I are the terminal voltage and the input current, and U_p is the polarization voltage from the simplified fractional order model. SOC_0 and SOC are the initial and current SOC. α is the fractional order. $C_{N,t}$ is the normal capacity under different pressures. η is the Coulomb efficiency. k is the current time. U_{oc} is the open-circuit voltage, which is a polynomial function of SOC. All model parameters of RC networks are a function of SOC and σ.

3.3.2. Fractional-order impedance models

This work establishes the fractional-order impedance model in the frequency domain [35] to investigate pressure-induced electrochemical reactions, encompassing elements such as ohmic resistance, cable inductance, electrochemical interfacial response, electrolyte diffusion, and solid diffusion processes. The model can be expressed as follows:

$$Z_{\mathrm{sim}}(s) = R_o + \frac{R_L}{1+\tau_L s} + \frac{R_i}{1+(\tau_i s)^{\alpha_1}} + \frac{R_e}{1+\tau_e s} + \frac{R_s}{s^{\alpha_2}} \tag{26}$$

where R_L and L represent the cables' resistance and inductance. R_o represents the ohmic resistance. R_i and τ_i are the resistance and capacitance at the solid–liquid phases interface. R_e and τ_e denote the liquid-phase diffusion resistance and capacitance. R_s is solid-diffusion resistance and the inverse of the Warburg coefficient. These model parameters have been identified using a multi-step, multi-objective genetic algorithm [27]. Importantly, all model parameters are influenced by pressure conditions. The simulated impedance considering these identified pressure-related parameters can be expressed as:

$$Z_{\mathrm{sim}}(s) = \frac{u_p(s)}{i(s)} = \frac{\sum_{j=1}^{12} b_j s^{\beta_j}}{\sum_{j=1}^{6} a_j s^{\alpha_j}} + R_o \tag{27}$$

where a, b, α, β represent the coefficients of the denominator and molecule parts. The detailed expressions of a, b, α, β were given in the supplementary file.

To achieve fast time-domain simulations, we describe the fractional-order transfer function in Eq. (27) using the Grünwald-Letnikov (G-L) definition [36,37]. To enhance computational efficiency without sacrificing precision, we select a truncation length denoted as N_{FOM}, set to 150.

By substituting GL definition into Eq. (27), we derive a discrete form for total polarization voltage:

$$u_p(t) = \left[B \cdot i(t-kh) + C \cdot i(t-kh) \cdot R_o + D \cdot u_p(t-kh)\right]/A$$
$$A = \sum_{j=1}^{6} \frac{a_j}{h^{\alpha_j}}, B = \sum_{k=0}^{N_{FOM}} \sum_{j=1}^{12} \frac{b_j}{h^{\beta_j}} w_k^{\beta}, C = \sum_{k=0}^{N_{FOM}} \sum_{j=1}^{6} \frac{a_j}{h^{\alpha_j}} w_k^{\alpha}, D = \sum_{k=1}^{N_{FOM}} \sum_{j=1}^{6} \frac{a_j}{h^{\alpha_j}} w_k^{\alpha} u_p(t-kh) \tag{28}$$

To minimize computational effort within our electromechanical model under FUDS, we simplify our time-domain fractional order model based on the EIS, focusing on specific frequency ranges: high-low frequencies characterized by an equivalent circuit of R(RQ)(RC)W; middle frequencies represented by R(RQ)(RC), R(RQ), and R(RC) in Table 3. The Akaike Information Criterion (AIC), grounded in information entropy principles, is employed to evaluate both goodness-of-fit and complexity for our models.

$$AIC = 2n - 2\log\left(\frac{1}{L}\sum_{i=1}^{N}(Y_{mea.} - Y_{sim.})^2\right) \quad (29)$$

where n is 1.5 when fractional order models are applied, while n is 1 when RC models are applied. Thus, this work selected an R(RC) model as the basic model. With the identified parameters, the total ohmic internal resistance of the battery R_0 can be extracted by adding ohmic and interfacial resistance.

3.3.3. Sensorless battery expansion estimation

To develop a sensorless battery expansion estimator, we utilize a discrete-time impedance model of the nonlinear system to describe the electromechanical coupled behavior of the battery:

$$\begin{cases} x_k = f(x_{k-1}, u_{k-1}) + \omega_{k-1} \\ y_k = g(x_{k-1}, u_{k-1}) + v_{k-1} \end{cases} \quad (30)$$

where $u_k = I_k$, $x_k = [SOC_k, U_{p,k}, \sigma_k]$, and $y_k = U_{t,k}$ are the system input, states, and output, respectively. Here, w_k and v_k denote the noise associated with system states and measurements, characterized by covariance matrices R_w and R_v. The state space equations for nonlinear discrete systems in Eq. (30) can be expressed as follows:

$$f(x_k, u_k) = \begin{bmatrix} SOC_k + I_k\Delta t/3600C_n \\ U_{p,k}e^{-\frac{\Delta t}{RC}} + I_kR\left(1 - e^{-\frac{\Delta t}{RC}}\right) \\ \sigma_k + \Delta\sigma_{s,BL}(SOC_k) \end{bmatrix} \quad (31)$$

$$g(x_k, u_k) = OCV(SOC_k, \sigma_k) + U_{p,k} + I_kR_o(SOC_k, \sigma_k) \quad (32)$$

To develop the real-time battery expansion observer, we linearize these nonlinear discrete systems using the Taylor series equation. This process transforms functions $f(x_k, u_k)$ and $g(x_k, u_k)$ into Jacobian matrices **F** and **G**, representing partial derivatives of f and g:

$$\boldsymbol{F}_k = \left.\frac{\partial f(x_k, u_k)}{\partial x_k}\right|_{x_k=\hat{x}_k^+, u_k} \quad \boldsymbol{G}_k = \left.\frac{\partial g(x_k, u_k)}{\partial x_k}\right|_{x_k=\hat{x}_k^+, u_k} \quad (33)$$

The coefficient matrices within the Jacobian matrix **F**, derived from partial derivatives of $f(x_k, u_k)$, are expressed as:

$$\boldsymbol{A}_k = \begin{bmatrix} 1 & 0 & 0 \\ 0 & \exp\left(-\frac{\Delta t}{R(\sigma_k)C(\sigma_k)}\right) & 0 \\ d\sigma_k/dSOC & 0 & 1 \end{bmatrix}, \quad \boldsymbol{B}_k = \begin{bmatrix} \Delta t/3600C_n \\ R(\sigma_k)\cdot\left[1 - \exp\left(-\frac{\Delta t}{R(\sigma_k)C(\sigma_k)}\right)\right] \\ 0 \end{bmatrix} \quad (34)$$

Similarly, leveraging the partial derivatives of $g(x_k, u_k)$, coefficient matrices **C** and **D** in the Jacobian matrix **G** are expressed as

$$\boldsymbol{C}_k = \begin{bmatrix} \frac{dOCV(SOC_k,\sigma_k)}{dSOC_k} & 1 & 0 \end{bmatrix}, \boldsymbol{D} = R_o(\sigma_k) \quad (35)$$

Considering the electromechanical coupling effects are present in model parameters as functions of SOC and σ, we incorporate pressure-dependent parameter spaces into the reduced-order impedance model. The electromechanical coupling model facilitates battery expansion estimation using the EKF. Table 4 outlines this process in three main steps following initialization: (1) propagation of a time step, (2) observation and update processes, and (3) propagation across multiple time steps. During the propagation phase for each time step, we compute state estimates, error covariances, and model-based simulated voltage, enabling us to predict prior knowledge. The observation and update processes include calculating the Kalman gain matrix along with measurement updates for both state estimation and error covariance updates. Estimation of battery expansion is performed over extended time scales due to a longer stress relaxation process compared to electrochemical processes. A SOC interval of 2.5% is selected for calculations. The SOC along with expansion estimates for the electrothermal system can be iteratively determined. The initial preload σ_{init} can be determined by configuring the pressure sensor or the relationship between R_0 and pressure.

Table 4
The EKF algorithm steps for sensorless battery expansion estimation.

Algorithm 2 Extended Kalman filter algorithm with EMCM calculation. States are initialized at the beginning of every discharge cycle. Expansion estimation is propagated over time intervals under the FUDS driving cycle.

Initialization at $\zeta = \zeta_0$
$\sigma_0 = \sigma_{init}, \Delta\sigma_0 = 0$
For $\mathscr{B} \in$ segments, **do**
  Initialization at the start of the segment
  $x_0 = E[x_0], \boldsymbol{P}_0 = E\left[(x_0 - \hat{x}_0)(x_0 - \hat{x}_0)^T\right]$
  For I, V, $\sigma \in \mathscr{B}$, **do**
    Propagation of time step
    State estimation matrix: $\hat{x}_k^- = \boldsymbol{A}_{k-1}\hat{x}_{k-1}^- + \boldsymbol{B}_{k-1}u_{k-1} + \omega_{k-1}$
    Error covariance matrix: $\boldsymbol{P}_k^- = \boldsymbol{A}_{k-1}\boldsymbol{P}_{k-1}^-\boldsymbol{A}_{k-1} + \boldsymbol{Q}_k$
    Measurement matrix:$y_k^- = \boldsymbol{C}_k\hat{x}_k^- + \boldsymbol{D}_ku_k + v_k$
    Observation and update
    Kalman gain matrix: $\boldsymbol{K}_k^- = \boldsymbol{P}_k^-\boldsymbol{C}_k^T\left(\boldsymbol{C}_k\boldsymbol{P}_k^-\boldsymbol{C}_k^T + \boldsymbol{R}_k\right)^{-1}$
    State estimation matrix:$\hat{x}_k = \hat{x}_{k-1}^- + \boldsymbol{K}_k\left(y_k - y_k^-\right)$
    Error covariance matrix: $\boldsymbol{P}_k = (\boldsymbol{E} - \boldsymbol{K}_k\boldsymbol{C}_k)\boldsymbol{P}_k^-$
    Propagation of multiple time steps
    For $\hat{x}_k - \hat{x}_{k-\Delta T} > 2.5\%$, **do**
    State estimation matrix: $\hat{\sigma}_k = \hat{\sigma}_{k-\Delta T} + \left.\frac{d\Delta\sigma_{s,BL}}{dSOC}\right|_{\hat{x}_{k-\Delta T}} \cdot (\hat{x}_k - \hat{x}_{k-\Delta T})$
    end for
  end for
end for

4. Results and discussion

4.1. Simulation and verification of data-driven mechanical model

4.1.1. Comparison of data-driven model with calibration model

To evaluate the proposed data-driven mechanical model against a calibrated benchmark, we focus on the 1C charging process, which allows for a clear assessment of battery stiffness due to the monotonicity of expansion behavior at this rate. As shown in Fig. 6(a), we employed a polynomial function to fit the relationship of battery stiffness and SOC under different initial pressures. As shown in Fig. 6(a), the results indicate a strong nonlinearity in battery stiffness to SOC and initial pressure between 0 and 0.1 MPa. Fig. 6(b) and 6(c) depict polynomial functions fitted to the stiffness values derived from both the pressure sensor and buffer layer, demonstrating high fitting accuracy characterized by low RMSE values and R^2 values approaching 1, indicating their strong dependence on pressure. In our analysis, both calibrated and data-driven models were utilized to fit the expansion force $\Delta\sigma_s$ during the 1C charging phase using testing dataset #2. The comparison results presented in Fig. 6(d) demonstrate that both models exhibit similar trends across all SOC regions; however, there are notable differences in their rates of increase. The calibrated model shows significant challenges in accurately calibrating the stiffness of each component, leading to discrepancies. The data-driven model effectively simulates $\Delta\sigma_s$ under all initial stress conditions, particularly outperforming the calibrated model during contraction phases at

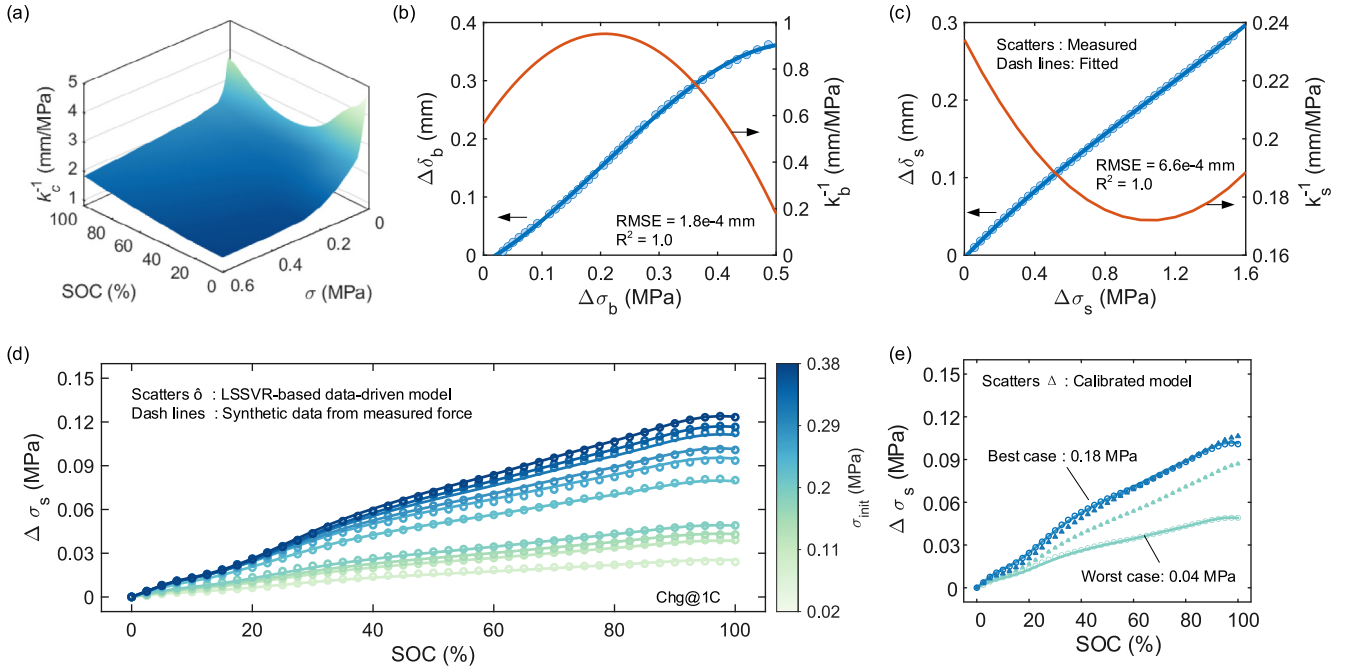

Fig. 6. Verification of the calibrated and data-driven model: (a) Stiffness map plot of the battery cell, Compressed stress, and thickness curve, as well as its stiffness curve of (b) buffer layer and (c) pressure sensor. (d) The comparison results of calibrated and LSSVR models under different initial stress. (e) The comparison of the best case in 0.18 MPa and the worst case in 0.04 MPa is in (d).

higher SOCs. In best cases, such as at an initial pressure of o.18 MPa, the calibrated $\Delta\sigma_s$ shows the highest accuracy across all pressures, further validating the effectiveness based on static stress–strain experiments. Conversely, the worst case is that the one at 0.04 MPa has a remarkable difference from the actual value due to inaccuracy calibration stiffness. The reason is the stress relaxation or creep caused by reciprocating pressurization and depressurization cycles over long-term operation. However, it is difficult and time-consuming to calibrate the stiffness of the buffer layer over aging. Thus, it is essential to establish a data-driven model with only measurable data during the charge and discharge process.

4.1.2. Comparison of data-driven model for different machine learning methods

To further validate the effectiveness of the proposed mechanical model, we compared the LSSVR-based mechanical model with other machine-learning methods, such as Elastic Net Regression (ENR), Random Forest (RF), Support Vector Regression (SVR), Gaussian Process Regression (GPR). As shown in Fig. 7(a), LSSVR exhibits high-fidelity fitting for nonlinear and non-monotonic expansion behavior, particularly during the contraction phase from H_2 to H_3 in high SOC regions, outperforming ENR and SVR in modeling complex mechanical properties. Fig. 7(a,b) show that LSSVR performs better than other methods in testing datasets #1 and #2, as indicated by scatter plots close to the actual value line. The MAPEs of all six models are listed in Table 5, showing that LSSVR achieves lower MAPE across all datasets compared to the others. Notably, GPR's MAPE is close to LSSVR's, while SVR performs significantly worse. The superior performance of LSSVR can be attributed to its efficient kernel function utilization and improved loss function with unconstrained optimization via Lagrange multipliers. Both LSSVM and GPR utilize kernel functions to achieve high-dimensional mapping and capture nonlinear relationships in data. While GPR explicitly performs probabilistic modeling, LSSVM exhibits implicit probabilistic characteristics through optimization and dual problem formulation. These similarities in kernel function use and probabilistic aspects result in comparable performance.

4.2. Voltage simulation and validation under FUDS driving cycle

4.2.1. Pressure dependence of electrical model parameters

To analyze the evolution of model parameters with pressure, we compare OCV-SOC curves under different pressures and present a 3D map plot of impedance parameters against SOC and pressure in Fig. 8(a). A significant difference in the OCV-SOC curve is observed between 0 MPa and 0.1 MPa, while there is almost no distinction at 0.03 MPa and 0.1 MPa. The OCV discrepancies at 0 MPa and 0.1 MPa occur primarily between 10% and 40% SOC, which can be attributed to pressure-induced changes in thermodynamic parameters, especially within phase transition regions dominated by silicon anode during lithiation – a phenomenon previously reported in [27]. As shown in Fig. 8(b), R_o increases with rising pressure across all SOCs, driven by the influence of electronic and ionic impedances under pressure conditions. The decrease in ionic impedance with increasing pressure enhances R_o, resulting from improved contact between electrodes and current collectors. In Fig. 8(c,d), both R_{inter} and R_e decrease due to an increase in electrochemical active surface area and reduced porosity. In Fig. 8(e) R_s remains relatively unchanged with pressure since the active material is not compressed. Additionally, the variation of τ with pressure does not align with the resistance changes due to differing trends in capacitance values. Notably, the variation of interfacial reaction parameter α_2 with pressure is more remarkable than that of solid-phase diffusion. The accuracy of model parameters reproduces the evolution of pressure-dependence electric model parameters, leading to high-fidelity voltage simulations under external pressures.

4.2.2. Simulation and verification of EMCM in preload conditions

To further validate the accuracy of the proposed model, we compared measured and simulated terminal voltages, along with

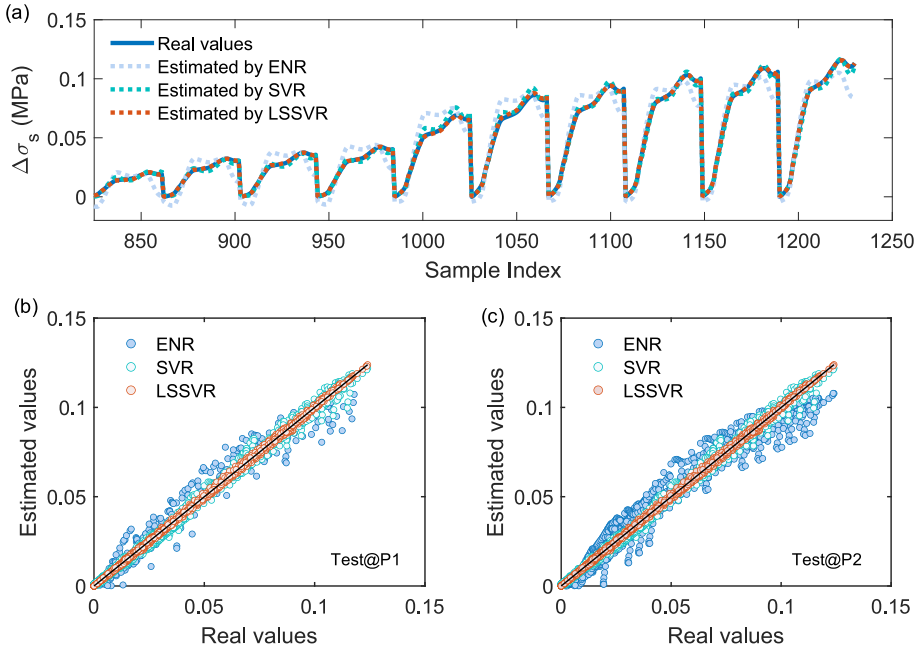

Fig. 7. Simulation and verification of data-driven mechanical model at (a) 0.1C discharge in testing dataset #2. (a) Testing dataset (b) #1, (c) #2.

Table 5
Validation results of different data-driven mechanical models.

MAPE (%)	ENR	RF	SVR	GPR	LSSVR
Training dataset	0.4511	0.0903	0.0941	0.0257	0.0181
Testing dataset #1	1.8093	0.3621	0.3775	0.0600	0.0423
Testing dataset #2	0.3906	0.0850	0.0830	0.0260	0.0218

their error distributions at 0.03 MPa and 0.05 MPa, as shown in Fig. 9. The simulated voltage under the FUDS aligns closely with the measured values presented in Fig. 9(a,c). In the zoomed-in portions of these figures, it is evident that the proposed model can effectively capture polarization changes under dynamic load currents in high SOC regions. As shown in Fig. 9(a,c), the absolute errors remain within −50 mV and 50 mV when SOC is above 10%. The error distribution graph further indicates that almost all absolute errors are concentrated within this range. However, for SOC values below 10%, absolute errors range between −120 mV and 100 mV in Fig. 9(b,d), which is significantly higher than those observed at SOC levels between 10% and 100%. This phenomenon can be attributed to incomplete fitting of the frequency-domain model at low SOCs. While enhancing the orders of equivalent circuit models could address this issue – as discussed in previous studies – this section, this work only explores pressure-related model parameters and which reactions cause more voltage errors in preload conditions. Thus, we don't discuss how to improve the simulation accuracy of the frequency-domain model in low SOCs.

4.2.3. Sensitivity analysis of pressure-induced model parameters

To further illustrate the necessity of updating model parameters with pressure, we compared the simulated voltage profiles using parameters from 0 MPa and 0.1 MPa against the measured voltage profile at 0.1 MPa in Fig. 10(a). The comparison of their MAPE and MAE is shown in Fig. 10(b). A notable discrepancy in voltage profiles was observed in Fig. 10(a), especially in the low SOC region. The absolute errors increase progressively with SOC, exceeding 200 mV at the discharging end, which can be attributed to differences in OCV between 0 MPa and 0.1 MPa. Updating parameters with pressure reduces MAPE by over 0.63% and MAE by more than 20 mV. To further analyze how these parameter updates contribute to total simulation error, we calculated MAE for different changes in model parameters, using the results from updating all parameters as a benchmark. The highest MAE was associated with OCV, confirming our previous speculation that OCV is a primary factor influencing voltage errors, as shown in Fig. 10(c,d). However, the effect of other parameters on output voltage is significantly less pronounced, with their influence ranked as follows: R_e, R_o, and τ_e. When these parameters are increased threefold in Fig. 10(e-g), we observe variations in errors across different SOC regions: R_e and τ_e predominantly affect the simulated voltage at high and low SOCs, respectively, while R_o influences simulated voltage across all SOC levels. The simulated results demonstrate the necessity of updating pressure-related model parameters – especially initial pressure rather than expansion force – since calibrated OCV and impedance parameters have substantial impact on output voltage during initial preload conditions, as shown in Fig. 10(a). This is particularly relevant given that expansion forces under flexible bracing modes are relatively low: less than 0.07 MPa at an initial pressure of 0.1 MPa and around 0.13 MPa at an initial pressure of 0.4 MPa. Thus, achieving high-precision calibration of OCV and impedance parameters at initial pressure is critical for improving real-time voltage simulations.

4.2.4. Robustness analysis of expansion estimation under multi-source errors

In the battery expansion estimation framework utilizing data-driven electromechanical models, the estimated SOC and calibrated values at initial pressure are important input information. However, these inputs are subject to algorithm estimation errors and pressure sensor measurement errors. To further analyze the

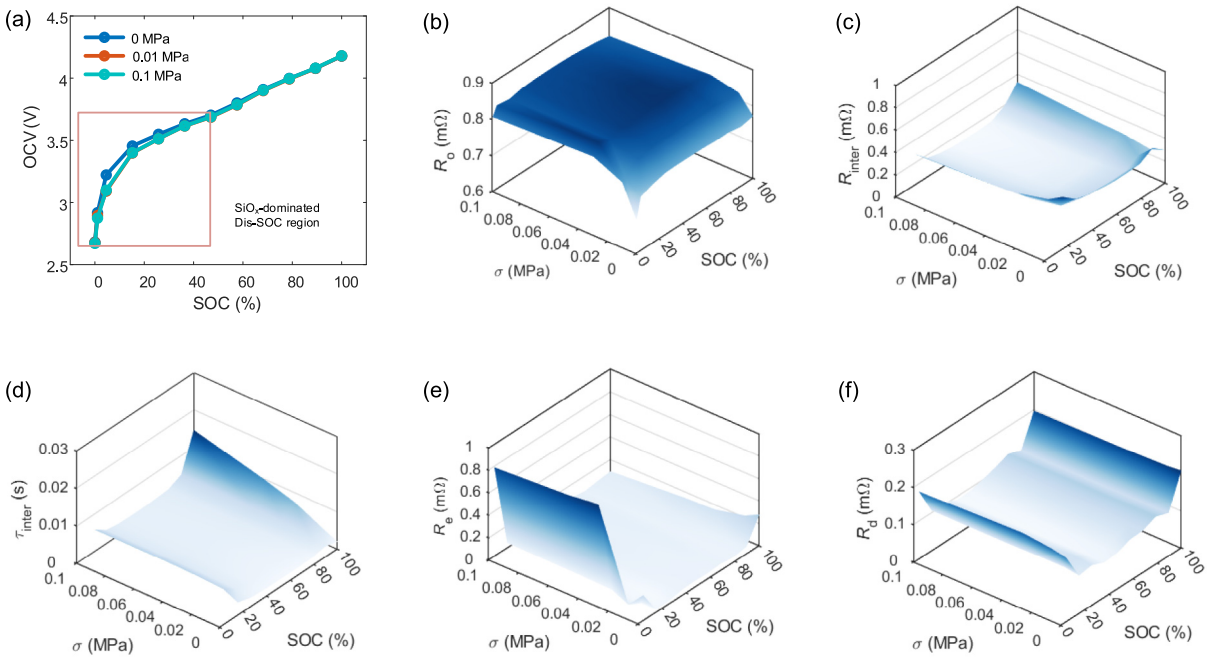

Fig. 8. Model parameters under different SOCs and pressures: (a) OCV, (b) R_o, (c) R_{inter}, (d) τ_{inter}, (e) R_e, (f) R_d.

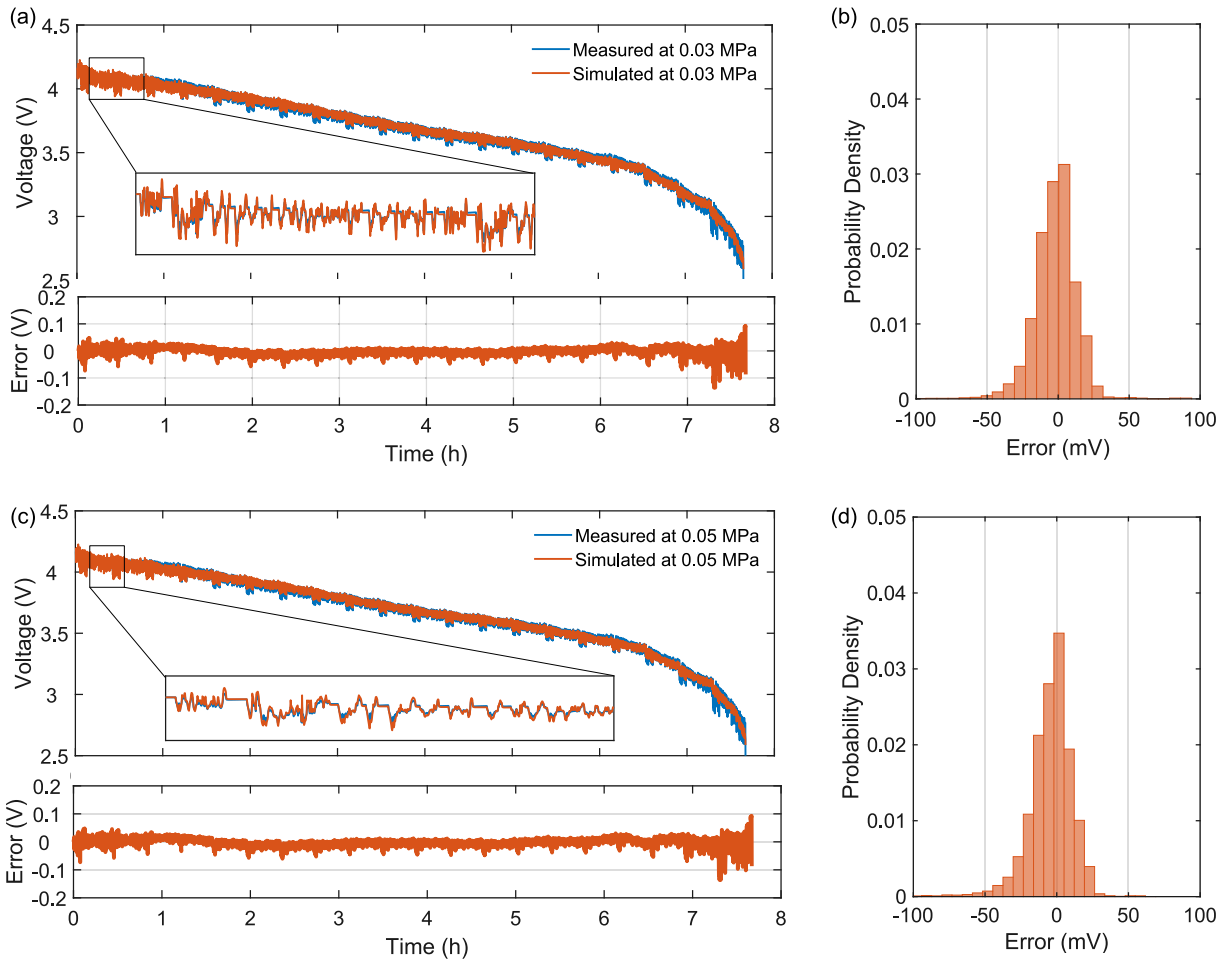

Fig. 9. The measured voltage, simulated voltage, and their error distribution at (a, b) 0.03 MPa and (c, d) 0.05 MPa.

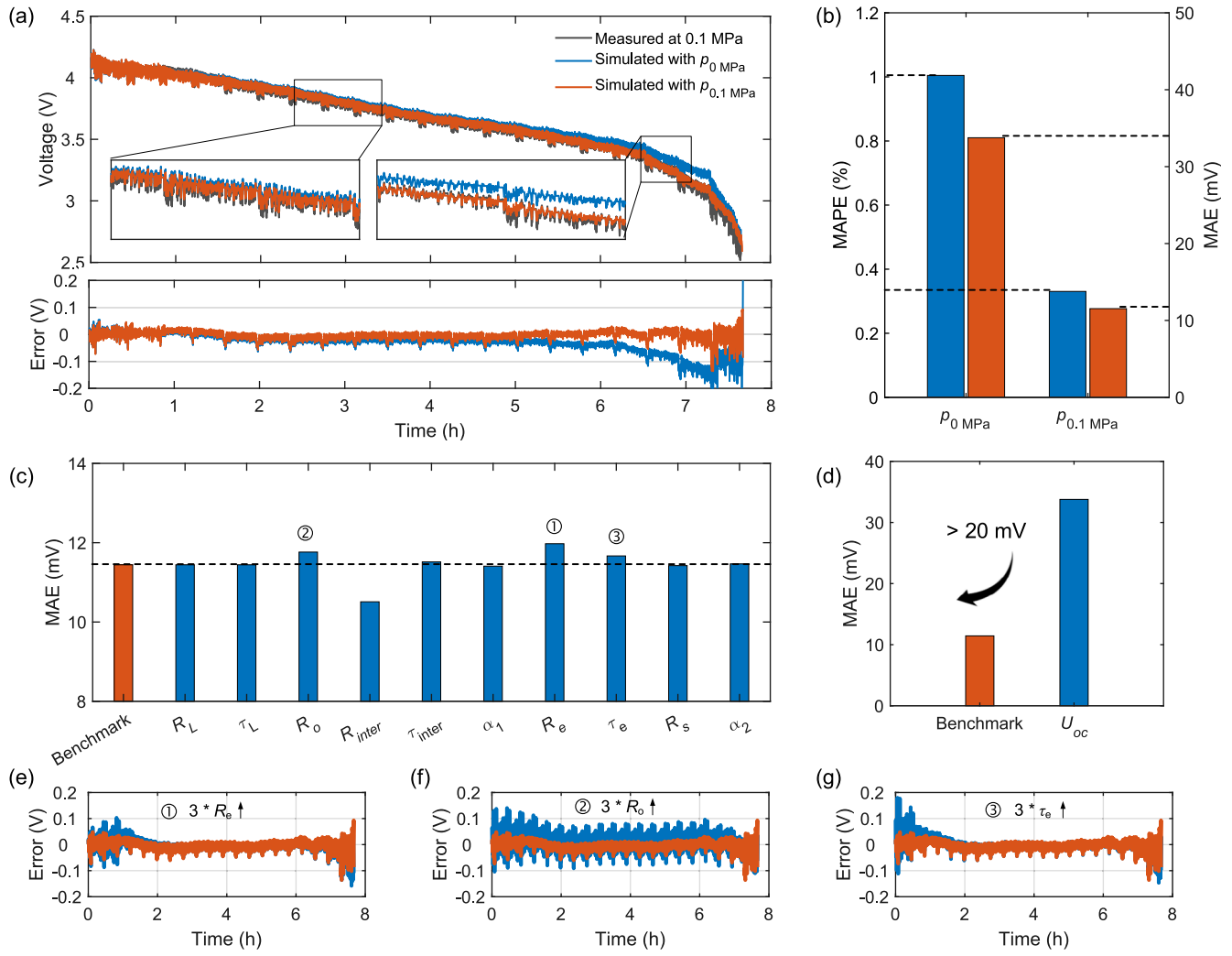

Fig. 10. Voltage simulation results under preload conditions. (a) Comparison results of measured voltage at 25 ℃ @ 0.1 MPa, simulated voltage with model parameters at 0.1 MPa ($p_{0.1\ MPa}$) and 0 MPa ($p_{0\ MPa}$), and the corresponding error. (b) MAPE and MAE with updated and un-updated parameters. The variation of MAE with updated (c) impedance parameters and (d) OCV at 25 ℃ @ 0.1 MPa. The error evolution with the changed (e) R_e, (f) R_o, and (g) τ_e with three times.

robustness of the proposed framework, we analyze how these influencing factors affect battery expansion estimation by artificially generating a dataset that incorporates SOC estimation errors and sensor measurement errors at different levels. Following the AIC evaluation of reduced-order models discussed in Table 6, we conducted a robustness analysis of battery expansion estimation using the generated dataset and reduced-order R(RC) model-based EKF algorithm described in Section 3.3.3.

4.2.5. Expansion estimation under estimated SOC errors

Four different noise levels with standard deviations were added to the normal data in the generation dataset for the model-based EKF estimators. This allowed us to analyze the model robustness under different scales of SOC estimation errors. We compared outcomes using normal data against those influenced by SOC estimation errors, which ranged from ± 1% to ± 5%, aligning with the standard error range reported by Xiong et al. [30]. These SOC estimation errors originate from updated model parameters with pressure and measurement errors in current and voltage signals. Fig. 11(a, b) indicate that SOC estimation maintains high accuracy (<2%) and rapid convergence capability (<100 s). Notably, SOC estimation errors associated with OCV-SOC curves at 0 MPa are higher than those at 0.1 MPa when external pressure is applied, highlighting the importance of updating OCV based on pressure for improving SOC estimation accuracy. These SOC estimation errors further lead to inaccuracies in battery expansion estimation. In Fig. 11(c, d), we observe that expansion estimation results, despite varying levels of SOC estimation errors, still track the general trends of expansion as SOC decreases. However, maximum absolute errors for both best and worst cases occur within the 80% to 100% SOC range, while another peak in absolute error arises between 20% and 30% SOC for worst-case scenarios. The RMSEs, MAPEs, and MAEs for the battery expansion estimation in the FUDS driving cycle are summarized in Table 7. The RMSEs, MAPEs, and MAEs for battery expansion estimates during the FUDS driving cycle are summarized in Table 7; all testing datasets exhibit MAPEs below 0.1% and MAEs under 3%, meeting industrial requirements for maximum state estimation errors such as those related to SOC.

The initial values of SOC and preload force are crucial for accurate expansion estimations under FBM. Any initial SOC error can be mitigated through an expansion estimation framework operating over longer time scales (e.g., using 2.5% SOC intervals), which far exceeds the convergence time of EKF when faced with inaccurate initial values. Moreover, initial pressure during charging can be monitored via pressure sensors during multi-cell stacking processes within battery modules. In contrast, long-term operational

Table 6
The simulated error of different impedance models in the time domain.

Models	RMSE (mV)	MAE (mV)	MAPE (%)	AIC
(RL)R(RQ)(RC)W	15.24	10.80	0.31	25.28
R(RQ)(RC)W	15.24	10.80	0.31	23.27
R(RQ)(RC)	16.46	11.54	0.33	21.06
R(RQ)	16.87	11.75	0.33	18.90
R(RC)	17.36	11.89	0.34	18.21

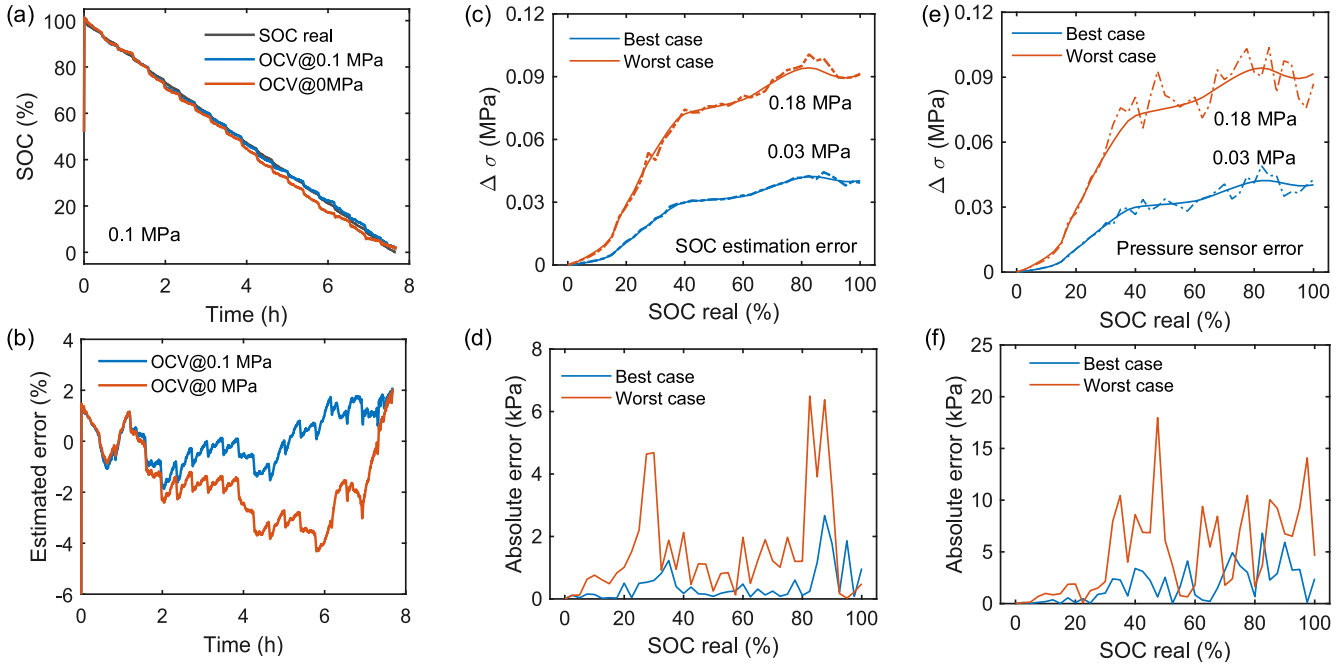

Fig. 11. (a) SOC estimation results and (b) their estimation error with OCV at 0 MPa and 0.1 MPa. The effect of SOC estimation error on (c) expansion results and (d) their absolute errors in best and worst cases. The influence of pressure sensor measurement error on (e) expansion results and (f) their absolute errors in best and worst cases.

Table 7
Validation of expansion estimation from SOC estimation errors.

Evaluation metrics	Normal	±1%	±2%	±4%	±6%
RMSE (kPa)	0.82	1.01	1.67	3.09	3.99
MAE (kPa)	0.58	0.75	1.09	1.80	2.35
MAPE (%)	0.022	0.025	0.035	0.046	0.060

data-driven models derive initial pressures under FUDS driving cycles, enhancing stability and accuracy. An interesting observation is presented in Fig. S2: battery expansion trends during a 0.1C discharge closely align with those observed during FUDS driving cycles due to similar long-term stress relaxation effects—typically exceeding five hours. Consequently, we opted to use data from a 0.1C discharge instead of FUDS driving cycles to minimize uncertainty introduced by random driving conditions.

4.2.6. Expansion estimation under different sensor noisy levels

To further analyze the model robustness under different scales of measurement errors, four different noise levels with standard deviations were added to the normal data in the calibrated dataset of different pressure sensors. These sensors, such as optical fiber, load cells, and thin-film pressure sensors, are typically used in practical scenarios for fault diagnosis. The sensor noise was simulated by adding a zero-mean white Gaussian noise, configured with the standard deviation (σ) from 1% to 5% of their initial point values to both calibrated pressure input sequences. With a 5% Gaussian noise level, the maximum deviation of 99.5% of the data is about 5% (3σ) of the actual pressure values, which matches the industrial requirement of the maximum measurement error for pressure sensors. The estimation performance of the LSSVR model for expansion behavior from noisy input sequences is shown in Fig. 11 (e,f). Adding noise to the input does not affect the overall trends for best and worst cases, but the error curves are not smooth. In best and worst cases, the noise does not almost influence estimation performance in the range of 0% ~ 35% SOC, guaranteeing the stability of the LSSVR model due to the highest gradient range. However, the measurement noise in both cases leads to severe estimation shaking around actual values in the SOC range from 35% to 100%. The absolute errors are less than 10 kPa and 20 kPa for 13 kPa and 180 kPa of initial preload, respectively. The maximum absolute errors are mainly concentrated in the 35–55% and 90% – 100% SOC range. The primary metrics of the model are summarized in Table 8. The RMSEs and MAEs for all cases are less than 6.5 kPa and 3 kPa, respectively, and MAPEs are less than 0.1%, which matches the requirement of state estimation in BMSs. These

Table 8
Expansion estimation results with different sensor noise levels.

Evaluation metrics	Normal	1%	2%	4%	5%
RMSE (kPa)	0.82	1.29	2.37	2.37	6.13
MAE (kPa)	0.58	0.80	1.43	1.43	3.49
MAPE (%)	0.022	0.025	0.035	0.035	0.068

phenomena indicate that the data-driven model can accurately estimate battery expansion. Various filters should be implemented to enhance the model performance and reduce the estimation errors to smooth the input data. Compared with SOC estimation errors, pressure measurement errors have a more significant influence on battery expansion estimation due to the high sensitivity of the model for calibrated pressure data under CDM.

4.2.7. Limitation and outlook

This work focuses on developing a data-driven mechanical model that takes into account C-rate, SOC, and preload force under flexible bracing conditions, such as buffer layers and deformation elements. The data-driven mechanical model will be extended to other chemistry with nonlinear expansion characteristics in the future. However, the effects of temperature and aging on battery expansion have not been thoroughly investigated due to the limitations posed by expensive mechanical and temperature characterization methods and the challenges associated with conducting long-term lifetime tests. While similar expansion characteristics have been observed during small current and dynamic condition discharges, it remains uncertain whether this similarity holds throughout the entire lifespan of the battery.

Another challenge identified is the low robustness of the proposed framework when subjected to pressure sensor measurement errors of 5%, especially considering that thin-film sensors commonly exhibit measurement errors of around 10% in mainstream production. Moving forward, we aim to enhance the data-driven mechanical model by incorporating additional dimensions and implementing advanced deep-learning algorithms with encoders. This will allow us to introduce more influencing factors related to battery expansion while improving the model's robustness against state estimation inaccuracies and sensor measurement errors. Ultimately, configuring pressure sensors alongside estimating the mechanical state offers advanced and effective solutions for battery fault diagnosis and safety warnings, contributing to improved reliability in battery management systems.

5. Conclusion

In this work, we designed a sensorless battery expansion estimation framework that utilizes cloud-assisted data-driven electromechanical coupled models within the EKF for onboard fault diagnosis and early warning, complemented by the configuration of pressure sensors. We conducted electrochemical and mechanical characterization experiments under various mechanical boundaries to reveal the electrochemistry of expansion and electromechanical coupling behavior through impedance models. The pressure-dependent OCV and impedance parameters significantly enhance simulated voltage accuracy, achieving an MAE of less than 20 mV and SOC estimation accuracy of about 2%. Sensitivity analysis of the full-order impedance model at 0 MPa and 0.1 MPa revealed the importance of OCV, electrolyte diffusion impedance R_e, and ohmic resistance R_o in improving voltage simulation, guiding the selection of a reduced-order model by sensitivity results and AIC metrics in real-time estimation. The mechanical constitutive equations under various mechanical boundaries were derived for the first time to explore the transformation relationship of expansion behavior influenced by the stiffness of each component within mechanical systems. A novel swelling coefficient was proposed to characterize the relationship between rigid or free and flexible bracing with a buffer layer. The force- and displacement-type expansion model was developed using swelling coefficient and calibrated data under CDM or CPM.

The data-driven mechanical model established in this work utilized SOC, current, and calibrated expansion force under CDM as inputs to estimate battery expansion across different preload levels. The model demonstrated an average mean absolute error of less than 1 kPa at all initial pressures ranging from 10 kPa to 400 kPa for battery expansion estimation, aligning well with industry standards. When compared to calibrated stiffness models and other machine learning approaches, the proposed LSSVR-based data-driven model exhibited superior performance in estimating expansion under varying pressures. We also validated the model against various levels of noisy input data, including SOC estimation errors and calibrated pressure measurement inaccuracies. The results confirmed the robustness of our model in handling SOC estimation and sensor measurement errors during battery expansion estimations.

In summary, the estimation framework presented in this work provides an effective solution for accurate sensorless expansion estimation using machine learning. This approach holds promise for future applications across more electrochemical systems, particularly those exhibiting nonlinear mechanical behaviors. Additionally, this work underscores the importance of precise battery estimation algorithms for state monitoring and fault diagnosis.

CRediT authorship contribution statement

Xue Cai: Writing – original draft, Methodology, Investigation, Conceptualization. **Caiping Zhang:** Writing – review & editing, Methodology, Funding acquisition. **Jue Chen:** Writing – review & editing, Software, Resources. **Zeping Chen:** Writing – review & editing, Investigation. **Linjing Zhang:** Investigation, Formal analysis. **Dirk Uwe Sauer:** Writing – review & editing, Validation. **Weihan Li:** Writing – review & editing, Supervision, Methodology, Funding acquisition.

Declaration of competing interest

The authors declare that they have no known competing financial interests or personal relationships that could have appeared to influence the work reported in this paper.

Acknowledgments

The National Science Fund supported this work for Excellent Youth Scholars of China (Grant No. 52222708) and the National Natural Science Foundation of China (Grant No. 51977007). Part of this work is supported by the research project "SPEED" (03XP0585) at RWTH Aachen University, funded by the German Federal Ministry of Education and Research (BMBF).

Appendix A. Supplementary material

Supplementary data to this article can be found online at https://doi.org/10.1016/j.jechem.2024.12.068.

References

[1] R. Shao, Z. Sun, L. Wang, J. Pan, L. Yi, Y. Zhang, J. Han, Z. Yao, J. Li, Z. Wen, S. Chen, S.-L. Chou, D.-L. Peng, Q. Zhang, Angew. Chem. 136 (2024) e202320183.
[2] C. Fan, K. Liu, Y. Ren, Q. Peng, J. Energy Chem. 92 (2024) 738–758.
[3] C. Han, Y. Gao, X. Chen, X. Liu, N. Yao, L. Yu, L. Kong, Q. Zhang, InfoMat 6 (2024) e12521.
[4] R. Li, W. Li, A. Singh, D. Ren, Z. Hou, M. Ouyang, Energy Storage Mater. 52 (2022) 395–429.
[5] V. Müller, R.-G. Scurtu, M. Memm, M.A. Danzer, M. Wohlfahrt-Mehrens, J. Power Sources. 440 (2019) 227148.
[6] S.S. Lee, T.H. Kim, S.J. Hu, W.W. Cai, J.A. Abell, Joining Technologies for Automotive Lithium-Ion Battery Manufacturing: A Review, in: ASME 2010 Int. Manuf. Sci. Eng. Conf. Vol. 1, ASMEDC, Erie, Pennsylvania, USA, 2010. Pp. 541–549.
[7] T. Deich, M. Storch, K. Steiner, A. Bund, J. Power Sources. 506 (2021) 230163.
[8] J. Cannarella, C.B. Arnold, J. Power Sources. 245 (2014) 745–751.
[9] P. Daubinger, M. Schelter, R. Petersohn, F. Nagler, S. Hartmann, M. Herrmann, G.A. Giffin, Adv. Energy Mater. 12 (2022) 2102448.
[10] W. Huang, Y. Ye, H. Chen, R.A. Vilá, A. Xiang, H. Wang, F. Liu, Z. Yu, J. Xu, Z. Zhang, R. Xu, Y. Wu, L.-Y. Chou, H. Wang, J. Xu, D.T. Boyle, Y. Li, Y. Cui, Nat. Commun. 13 (2022) 7091.
[11] Y. Wang, C. Zhang, J. Hu, P. Zhang, L. Zhang, Z. Xu, J. Power Sources. 587 (2023) 233673.
[12] S. Chen, X. Wei, G. Zhang, X. Rui, C. Xu, X. Feng, H. Dai, M. Ouyang, Renew. Sustain. Energy Rev. 187 (2023) 113740.
[13] S. Chen, X. Wei, G. Zhang, X. Wang, X. Feng, H. Dai, M. Ouyang, J. Power Sources. 580 (2023) 233397.
[14] W. Zhou, Electrochim. Acta 185 (2015) 28–33.
[15] S. Mohan, Y. Kim, J.B. Siegel, N.A. Samad, A.G. Stefanopoulou, J. Electrochem. Soc. 161 (2014) A2222–A2231.
[16] K.-Y. Oh, B.I. Epureanu, J. Power Sources. 365 (2017) 220–229.
[17] Y. Yi, C. Xia, L. Shi, L. Meng, Q. Chi, L. Qian, T. Ma, S. Chen, Energy 292 (2024) 130541.
[18] Y. Jiang, J. Xu, W. Hou, X. Mei, Energy 221 (2021) 119804.
[19] P. Xu, J. Li, Q. Xue, F. Sun, J. Energy Storage. 50 (2022) 104559.
[20] B. Jiang, S. Tao, X. Wang, J. Zhu, X. Wei, H. Dai, Energy 278 (2023) 127890.
[21] E. Kwak, S. Jeong, J. Kim, K.-Y. Oh, J. Power Sources. 483 (2021) 229079.
[22] S. Hahn, S. Theil, J. Kroggel, K.P. Birke, J. Energy Storage. 40 (2021) 102517.
[23] E. Kwak, D.S. Son, S. Jeong, K.-Y. Oh, J. Energy Storage. 28 (2020) 101269.
[24] O. Von Kessel, T. Deich, S. Hahn, F. Brauchle, D. Vrankovic, T. Soczka-Guth, K.P. Birke, J. Power Sources. 508 (2021) 230337.
[25] K. Fan, Y. Wan, B. Jiang, J. Process Control. 112 (2022) 1–11.
[26] Y. Zheng, Y. Che, X. Hu, X. Sui, R. Teodorescu, IEEEASME Trans. Mechatron. (2024). https://doi.org/10.1109/tmech.2024.3367291.
[27] X. Cai, C. Zhang, Z. Chen, L. Zhang, D. Uwe Sauer, W. Li, J. Energy Chem. 95 (2024) 364–379.
[28] Y. Gao, N. Yao, X. Chen, L. Yu, R. Zhang, Q. Zhang, J. Am. Chem. Soc. 145 (2023) 23764–23770.
[29] Y. Gao, Y. Yuan, S. Huang, N. Yao, L. Yu, Y. Chen, Q. Zhang, X. Chen, Angew. Chem. Int. Ed. (2024). https://doi.org/10.1002/ange.202416506.
[30] A.J. Louli, J. Li, S. Trussler, C.R. Fell, J.R. Dahn, J. Electrochem. Soc. 164 (2017) A2689–A2696.
[31] H. Laufen, S. Berg, J. Engeser, M. Strautmann, A. Koprivc, C. Rahe, E. Figgemeier, D.U. Sauer, Adv. Mater. Technol. 9 (2024) 2301965.
[32] D. Sauerteig, N. Hanselmann, A. Arzberger, H. Reinshagen, S. Ivanov, A. Bund, J. Power Sources. 378 (2018) 235–247.
[33] T.R. Garrick, K. Kanneganti, X. Huang, J.W. Weidner, J. Electrochem. Soc. 161 (2014) E3297.
[34] L. Hoegaerts, J.A.K. Suykens, J. Vandewalle, B. De Moor, A Comparison of Pruning Algorithms for Sparse Least Squares Support Vector Machines, in: N.R. Pal, N. Kasabov, R.K. Mudi, S. Pal, S.K. Parui (Eds.), Neural Inf. Process., Springer, Berlin, Heidelberg, 2004, pp. 1247–1253.
[35] X. Cai, C. Zhang, H. Ruan, Z. Chen, L. Zhang, D.U. Sauer, W. Li, Adv. Sci. 11 (2024) 2406934.
[36] Y. Zheng, Z. Shi, D. Guo, H. Dai, X. Han, J. Power Sources. 489 (2021) 229505.
[37] H. Ruan, B. Sun, J. Jiang, W. Zhang, X. He, X. Su, J. Bian, W. Gao, Electrochim. Acta 394 (2021) 139066.